

Electron acceleration in non-relativistic quasi-perpendicular collisionless shocks

Rui Xu and Anatoly Spitkovsky

Department of Astrophysical Sciences, Peyton Hall, Princeton University, Princeton, NJ, 08544

Damiano Caprioli

Department of Astronomy and Astrophysics, University of Chicago, 5640 S. Ellis Ave, Chicago, IL 60637

We study diffusive shock acceleration (DSA) of electrons in non-relativistic quasi-perpendicular shocks using self-consistent one-dimensional particle-in-cell (PIC) simulations. By exploring the parameter space of sonic and Alfvénic Mach numbers we find that high Mach number quasi-perpendicular shocks can efficiently accelerate electrons to power-law downstream spectra with slopes consistent with DSA prediction. Electrons are reflected by magnetic mirroring at the shock and drive non-resonant waves in the upstream. Reflected electrons are trapped between the shock front and upstream waves and undergo multiple cycles of shock drift acceleration before the injection into DSA. Strong current-driven waves also temporarily change the shock obliquity and cause mild proton pre-acceleration even in quasi-perpendicular shocks, which otherwise do not accelerate protons. These results can be used to understand nonthermal emission in supernova remnants and intracluster medium in galaxy clusters.

Non-thermal particles are ubiquitous in the Universe. The acceleration of these particles is often associated with collisionless shocks. For instance, it is widely regarded that supernova remnant (SNR) shocks are responsible for the acceleration of galactic cosmic rays (CRs) up to the knee $E \sim 10^{17}$ eV (e.g., [1]). The dominant acceleration mechanism is the so-called diffusive shock acceleration (DSA, [2–5]), where particles gain energy by repeatedly crossing the shock while scattering off converging magnetic perturbations on both sides. The final momentum distribution $f(p)$ is a universal power-law with index $f(p) \propto p^{-3r/(r-1)}$, where r is the shock compression ratio. For strong shocks with $r = 4$, the momentum distribution follows $f(p) \propto p^{-4}$.

While DSA naturally produces power-law distributions, it works only for particles whose Larmor radius is larger than the shock transition width, which is typically of the order of proton gyro-radius. One of the most important questions in CR physics, known as the injection problem, is how particles are extracted from the thermal pool to participate in DSA. Achieving injection energy is more challenging for electrons due to their smaller Larmor radii, compared to protons. Also, the shock potential barrier is tuned to reflect upstream ions, which hinders electron reflection [6].

Proton and electron injection for non-relativistic *quasi-parallel* shocks, where the angle between the background magnetic field and the shock normal is $\theta < 45^\circ$, have been studied with fully kinetic PIC simulations that show both species successfully injected into DSA [7, 8]. For *quasi-perpendicular* shocks ($\theta > 45^\circ$), proton acceleration and reflection into the upstream has been shown to be inefficient without pre-existing upstream turbulence ([6, 9, 10]). In quasi-perpendicular shocks with low sonic Mach numbers, electron scattering was reported to be mediated by oblique electron firehose instability driven by electrons reflected from the shock [11, 12]. Electron

pre-acceleration was also observed in perpendicular and quasi-perpendicular multi-dimensional PIC simulations [13, 14]. However, previous studies have not shown compelling evidence of DSA spectra forming downstream of quasi-perpendicular shocks.

In this Letter, we use kinetic simulations to study the formation of DSA power-law $f(p) \propto p^{-4}$ for electrons downstream of quasi-perpendicular shocks. This is the first report of a successful electron injection into DSA in quasi-perpendicular collisionless shocks in the absence of substantial proton acceleration. We demonstrate how electrons are extracted from the thermal pool and injected into DSA by scattering on electron-driven waves in the upstream. Finally, we discuss the effect of sonic and Alfvénic Mach numbers on the downstream electron spectrum.

We performed numerical simulations with the electromagnetic PIC code TRISTAN-MP [15]. To enable long integration times, the simulation domain is 1D along \hat{x} direction, retaining all components of fields and velocities. The setup is very similar to previous PIC simulations of collisionless shocks (e.g., [8, 16, 17]). In order to facilitate the analysis of upstream waves, the simulations are performed in the upstream rest frame by moving the left conducting boundary wall into stationary plasma. The resolution of our reference run is 10 cells per electron skin depth, c/ω_{pe} , where c is the speed of light and $\omega_{pe} = \sqrt{4\pi n e^2/m_e}$ is the electron plasma frequency (e , n and m_e are electron charge, number density and mass, respectively). The simulation domain is enlarged by expanding the right boundary with time to save computational resources, with the final domain size reaching $\sim 3.5 \times 10^4 c/\omega_{pe}$. We use 256 particles per cell per species with a reduced proton-to-electron mass ratio $m_p/m_e = 100$. The wall velocity is fixed at $v_0 = 0.15c$. Upstream protons and electrons are assumed to be in thermal equilibrium with temperature

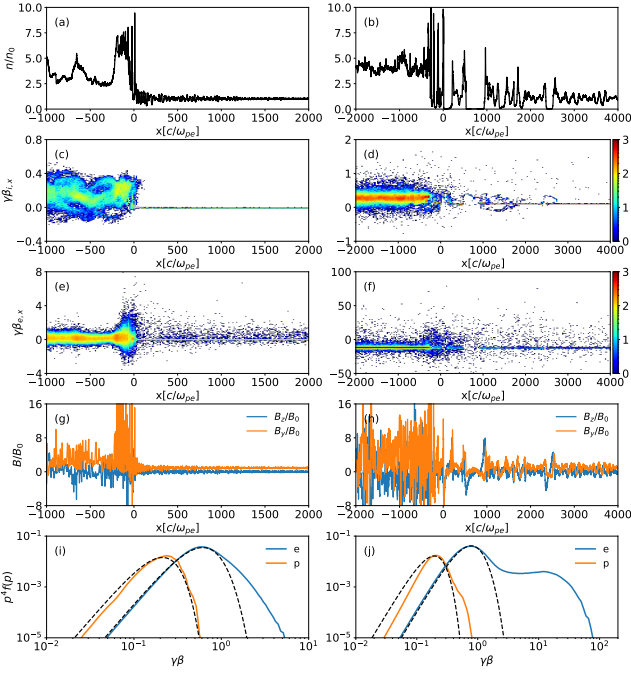


FIG. 1. Structure of quasi-perpendicular shock ($\theta = 63^\circ$, M_s and $M_A \sim 60$) at simulation time $\sim 10\Omega_{cp}^{-1}$ (left panels) and $\sim 45\Omega_{cp}^{-1}$ (right panels): (a-b) electron number density normalized by the upstream value; (c-f) proton and electron $x - p_x$ phase space distribution $f(p_x)$; (g-h) \hat{y} and \hat{z} components of the magnetic field normalized by the background magnetic field; (i-j) downstream electron and proton spectra, where the dashed lines represent thermal Maxwellian distributions.

$T_p = T_e = 4 \times 10^{-4} m_e c^2$. The corresponding sonic Mach number is $M_s = v_{sh}/\sqrt{\gamma(T_p + T_e)/m_p} \approx 55$ for adiabatic index $\gamma = 5/3$. The Alfvénic Mach number is $M_A = v_{sh}/v_A \approx 63$, where $v_A = B_0/\sqrt{4\pi n m_p}$ is the Alfvén speed for the initial magnetic field, $\mathbf{B}_0 = B_0(\cos\theta\hat{\mathbf{x}} + \sin\theta\hat{\mathbf{y}})$, inclined at an angle $\theta = 63^\circ$ relative to the shock normal, so the shock is quasi-perpendicular.

Figure 1 shows the shock structure at time $t \approx 3.2 \times 10^4 \omega_{pe}^{-1} \approx 10\Omega_{cp}^{-1}$ (left panels) and at the final time $t \approx 45\Omega_{cp}^{-1}$ (right panels), where $\Omega_{cp} = eB_0/m_p c$ is the proton-cyclotron frequency. Electron number density (Fig. 1a,b) is compressed by a factor of $r \approx 4$ in the far downstream region, as expected. The density overshoot at the shock is attributed to gyrating protons undergoing coherent motion (e.g., [18, 19]). In Fig. 1(c-f), we show the proton and electron $x - p_x$ phase space distribution. Protons are reflected by the potential barrier at the shock, but due to magnetic obliquity they cannot escape far upstream (Fig. 1c). Unlike protons, the reflected electrons can outrun the shock. The energy gain from the magnetic mirror effect increases the projected velocity along the shock normal, which can be larger than the shock propagation speed [20, 21]. The reflected electrons preferentially move along the background magnetic

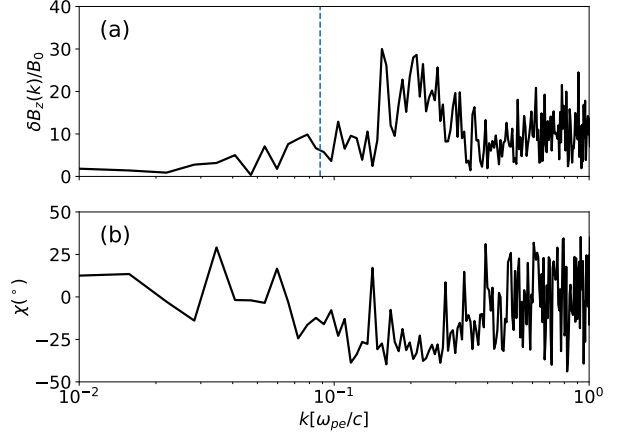


FIG. 2. (a) Fourier transform of B_z in the shock far upstream. Dashed line indicates the inverse of the mean gyroradius of reflected electrons. (b) Polarization angle χ of the upstream wave, where $\chi = \pm 45^\circ$ corresponds to right-(left-)handed circularly polarized modes. The wave is left hand circularly polarized and thus, non resonant with electrons.

field and contribute a net current along the magnetic field lines. The electron current drives strong waves in the upstream field which can scatter electrons back to the shock (see Fig. 1g,h). Figures 1(i-j) show the downstream electron and proton spectra. We see electrons successfully injected into DSA while protons only form a steep non-thermal tail.

To study the nature of such electron-driven waves, we perform Fourier analysis of the z-component of magnetic field in this region, as shown in Fig. 2a. The spectral energy density peaks at $k \simeq 0.2 \sim 0.3\omega_{pe}/c$, while the inverse of the mean gyroradius of reflected electrons is $k \lesssim 0.1\omega_{pe}/c$ [see dashed line in Fig. 2a]. Figure 2(b) shows the wave polarization angle $\chi = 0.5 \times \sin^{-1}(\mathbf{V}/\mathbf{I})$, where \mathbf{I} , \mathbf{V} are the Stokes parameters for the two transverse magnetic field components. The angle $\chi = \pm 45^\circ$ corresponds to a right-(left-)handed circularly polarized wave. We see that the wave is left-hand circularly polarized and, thus, non-resonant with electrons. After the fastest-growing mode saturates, we observe the migration of power to longer wavelengths [e.g., 22, 23]. While a small fraction of reflected protons is observed in the shock upstream at later times, the current carried by protons is less than ten percent of the electron current and does not affect the wave nature significantly. Thus, we conclude that the waves in the upstream are non-resonant waves driven by returning electrons via a Bell-like instability.

In order to illustrate how electrons are injected from the thermal pool, we track individual particles along their trajectories in real space and momentum space. Figure 3 shows the space-time and space-energy plots of two typical electrons that are injected into DSA. Electrons are initially reflected off the shock due to magnetic mirroring at time $t \approx 0.6 \times 10^5 \omega_{pe}^{-1}$. They remain trapped between

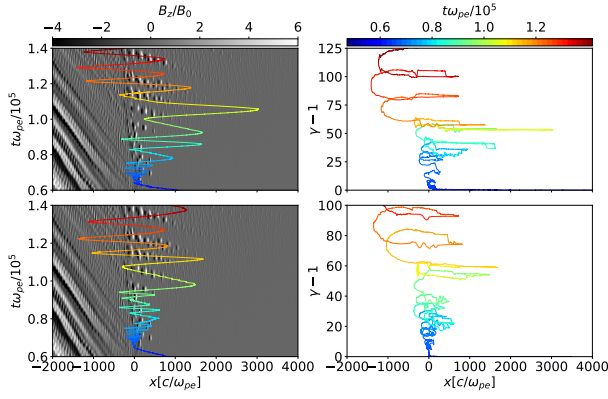


FIG. 3. Electron trajectories in the space-time (left panels) and the space-energy (right panels) plots. Both electrons are injected into DSA after multiply cycles of SDA. The gray-scale color map indicates normalized z-component of the magnetic field. The color line indicates time, as in the legend.

the shock front and the upstream waves and repeatedly undergo cycles of shock-drift acceleration (SDA) between $t \sim 0.6 - 0.8 \times 10^5 \omega_{pe}^{-1}$. At each encounter with the shock front, electrons undergo a new cycle of SDA and gain energy vigorously. The interplay between SDA and upstream wave scattering continues accelerating electrons and transits to standard DSA when electron momentum reaches $p_{inj} \approx 30 - 80 m_e c$. At this stage electrons diffuse in the upstream/downstream and the energy gain is from the interaction with upstream/downstream waves instead of the interaction with the shock. The acceleration process is very similar to electron injection in non-relativistic quasi-parallel shocks [8]; the major difference is that electrons are scattered by the non-resonant waves driven by returning electrons instead of returning protons.

Figure 4 shows the downstream electron and proton spectra for different Mach numbers as a function of time. The spectrum is multiplied by p^4 to emphasize the expected DSA scaling. Fig. 4(l) shows the downstream spectrum from our reference run, where electrons develop a power-law tail with spectral index 4, consistent with DSA prediction (cf. Fig. 1h). In this case, electron acceleration is very efficient: the downstream energy fraction in non-thermal electrons is $\epsilon_e \sim 7\%$ and increases to $\sim 10\%$ by the end of the simulation. Also, the maximum electron energy grows roughly linearly with time and eventually exceeds the maximum energy of downstream thermal ions. Similar to acceleration in quasi-parallel shocks, electrons show a typical DSA spectrum even in the range of momenta where they undergo SDA, indicating that the balance between energy gain and escape probability per cycle is more similar to DSA than to SDA [8]. Downstream protons are mostly thermal with a steep non-thermal tail, which is caused by the strong electron-driven upstream waves that temporarily change the shock obliquity and allow a small fraction of protons

to escape into the upstream. These protons are eventually advected downstream and form a steep spectrum.

Figures 4(a-k) show the same spectra as Fig. 4(l) but for different M_s and M_A . In these simulations, the left wall velocity is fixed at $v_0 = 0.15c$, and we change M_s by varying the plasma temperature and M_A by varying the background magnetic field strength. All other parameters are the same as in our reference run. We see that electrons are eventually injected into DSA in high Mach number quasi-perpendicular shocks (with both high M_s and M_A). For shocks with low M_s or M_A , reflected electrons also gain energy via SDA and contribute a similar upstream current but do not enter DSA at the end of the simulation. The acceleration efficiency depends on whether the reflected electrons are able to drive waves of large enough amplitude in the upstream. The amplitudes of upstream magnetic fluctuations near shocks for different Mach numbers are shown in the top right corner of each panel in Fig. 4. Large Mach number and especially large M_A shocks are able to drive strong upstream magnetic fluctuations with $\delta B/B_0 > 1$ which are responsible for scattering reflected electrons. For low M_A shocks in hot plasma (e.g., Fig. 4a), downstream electron spectrum develops a non-thermal SDA tail. Due to small amplitude waves in the upstream, we do not observe electron injection into DSA at the end of the simulation. Non-resonant instability is dominant when the energy density in the reflected electrons is larger than the energy density in the background magnetic field [24], which constrains $M_A > \sqrt{(1/2\epsilon_{e,up})(m_i/m_e)(v_{sh}/v_{dr})} \sim 10$, for the parameters measured in the near upstream, where $\epsilon_{e,up}$ is the fraction of reflected electrons and v_{dr} is the average drift velocity of the reflected electrons. Indeed, we see weak waves in $M_A \sim 11$ shocks, and the amplitude of the waves increases with the M_A . For realistic mass ratio, the extrapolated M_A needed for electron injection into DSA may be even higher, consistent with Mach numbers of several hundred expected in SNR shocks. Thermal effects also reduce the growth-rate of the instability, suppressing the waves in warmer plasmas [25, 26]. Thus, the current-driven instability favors high M_s and M_A shocks.

In addition to Mach numbers, the efficiency of electron acceleration also depends on the shock obliquity, and is much higher in quasi-perpendicular shocks compared to quasi-parallel shocks. In the quasi-perpendicular shocks presented in this Letter, $\epsilon_e \sim 0.7\%$ for Mach number ~ 30 (see Figure 4h). For quasi-parallel shocks, most of the energy goes into accelerated ions and $\epsilon_e \lesssim 0.1\%$ for Mach number ~ 20 (see Fig. 4 in [8]). This higher acceleration efficiency can be attributed to the magnetic mirror effect: electrons are more effectively reflected to the upstream in quasi-perpendicular shocks compared to quasi-parallel shocks, where the mirroring of electrons is mediated by the upstream turbulence driven by reflected protons. Also, at higher magnetic inclinations electron DSA has to vanish when obliquity approaches superlumi-

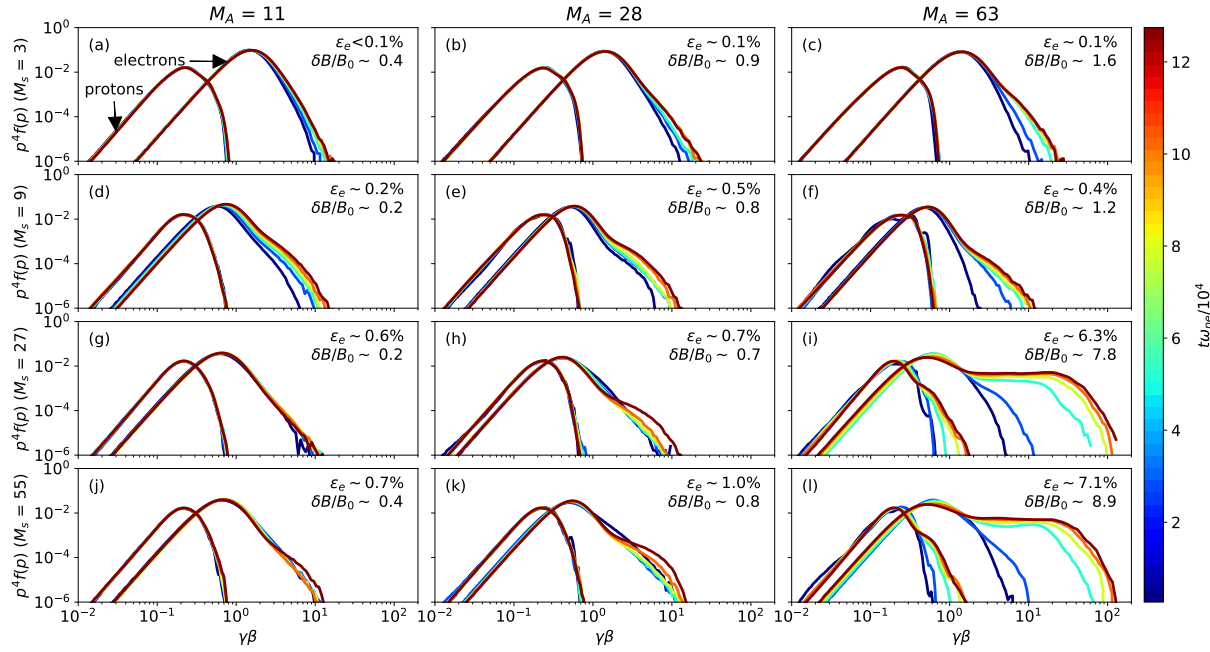


FIG. 4. Downstream electron and proton spectra as a function of time for different M_s and M_A for quasi-perpendicular shocks with angle $\theta = 63^\circ$ and $m_i/m_e = 100$. The spectrum is multiplied by p^4 to emphasize the scaling law expected in DSA. The color lines indicate time, as in the legend. The number fraction of non-thermal electrons ϵ_e at the end of the simulations, and the level of upstream magnetic fluctuations $\delta B/B_0$ are shown at the top right corner of each panel. Only shocks with $M \gg 1$ are able to produce large amplitude fluctuations with $\delta B/B_0 > 1$, and in these cases electrons are injected into DSA after multiple cycles of SDA and scattering of upstream waves.

nal shocks because fewer particles can outrun the shock; we expect the optimal angles for electron acceleration to lie between 60° and 70° . The critical superluminal angle becomes smaller as shocks become relativistic, $v_{sh} \rightarrow c$.

We can use these findings to interpret the morphology of nonthermal emission from supernova remnants. Some SNRs (e.g., SN1006) show bilateral symmetry in their synchrotron emission, which is understood as being due to pre-existing large-scale magnetic field in the remnant [e.g., 27]. In regions where the shock is quasi-parallel, ions are effectively injected into DSA and drive prominent magnetic field amplification with $\delta B/B_0 \gg 1$, but ϵ_e may be $\lesssim 0.1\%$ [8, 28]; in these quasi-parallel regions electrons can be accelerated to multi-TeV energies, which results in non-thermal X-ray emission. In regions where the shock is quasi-perpendicular, instead, ions are not injected and the magnetic field is not effectively amplified; electron acceleration can still occur with $\epsilon_e \sim 5 - 7\%$, as in our calculations, but up to smaller energies than in quasi-parallel regions, since $\delta B/B_0 \gtrsim 1$. This is consistent with the fact that quasi-perpendicular regions are radio-bright but not X-ray bright [29]. Finally, the relative radio brightness between parallel and perpendicular regions is determined by both ϵ_e and $\delta B/B_0$.

An important result of this study is the existence of shocks that preferentially accelerate electrons and not ions. This helps to reduce the tension of non-

detection of hadronic gamma-ray emission in galaxy clusters: the electrons responsible for the observed radio emission could be efficiently accelerated in high M_A quasi-perpendicular shocks, which do not efficiently accelerate protons. This would suppress secondary hadronic gamma-ray production. Upstream fluctuations are weaker for high M_A , low M_s shocks, which are commonly found in clusters of galaxies [30]. According to our simulations, such shocks accelerate electrons at a lower rate, with steep power-laws. However, these shocks reflect electrons into the upstream at nearly the same rate as high M_s shocks. Thus, we expect that even these weaker upstream waves may be sufficient to eventually inject electrons into DSA on substantially longer timescales. This could explain the observations where relativistic electrons produce radio “relics” in galaxy clusters, in structures that have inferred quasi-perpendicular magnetic geometry [31–33].

The results in this Letter were obtained using 1D PIC simulations and should be tested in multi-dimensions. Typically, multi-dimensional simulations allow for larger variability of magnetic inclination at the shock (e.g., due to shock corrugation), and this can reduce the average efficiency of electron injection. Our preliminary results show that 2D runs with out-of-plane background B field better represent fully 3D injection than in-plane simulations [cf. 14]. Since 1D simulations capture the essence

of the out-of-plane field dynamics, it is likely that our 1D results will remain relevant in 3D. The comparison with 1D simulations should be done with sufficiently large number of particles per cell to avoid artificial cooling of high-energy electrons due to discreteness effects in PIC simulations [34]. In addition, most of our simulations were done with an artificial mass ratio of 100. We have done limited simulations at $m_i/m_e = 400$, and find that the early properties of the shocks, including the reflected electron fraction, are not sensitive to the mass ratio. However, higher mass ratio simulations require higher Alfvénic Mach numbers in order to drive the upstream waves with electrons and reach the injection into DSA. These issues make a proper comparison with 1D simulations quite challenging numerically; we plan to present this in an upcoming study.

This research was supported by NSF (grants AST-1814708, AST-1714658) and by NASA (grants NNX17AG30G and 80NSSC18K1726). The simulations in this paper were performed using computational resources at the TIGRESS high-performance computer center at Princeton University. AS is supported by Simons Foundation (grant 267233).

-
- [1] T. K. Gaisser, R. Engel, and E. Resconi, *Cosmic Rays and Particle Physics* (Cambridge University Press, 2016).
 - [2] A. R. Bell, *MNRAS* **182**, 147 (1978).
 - [3] R. D. Blandford and J. P. Ostriker, *Astrophys. J.* **221**, L29 (1978).
 - [4] L. O. Drury, *Reports on Progress in Physics* **46**, 973 (1983).
 - [5] R. Blandford and D. Eichler, *Physics Reports* **154**, 1 (1987).
 - [6] D. Caprioli, A.-R. Pop, and A. Spitkovsky, *Astrophys. J.* **798**, L28 (2015), arXiv:1409.8291 [astro-ph.HE].
 - [7] T. N. Kato, *Astrophys. J.* **802**, 115 (2015), arXiv:1407.1971 [astro-ph.HE].
 - [8] J. Park, D. Caprioli, and A. Spitkovsky, *Phys. Rev. Lett.* **114**, 085003 (2015).
 - [9] D. Caprioli and A. Spitkovsky, *Astrophys. J.* **783**, 91 (2014).
 - [10] D. Caprioli, H. Zhang, and A. Spitkovsky, *JPP* (2018), arXiv:1801.01510 [astro-ph.HE].
 - [11] X. Guo, L. Sironi, and R. Narayan, *Astrophys. J.* **794**, 153 (2014), arXiv:1406.5190 [astro-ph.HE].
 - [12] X. Guo, L. Sironi, and R. Narayan, *Astrophys. J.* **797**, 47 (2014), arXiv:1409.7393 [astro-ph.HE].
 - [13] Y. Matsumoto, T. Amano, T. N. Kato, and M. Hoshino, *Phys. Rev. Lett.* **119**, 105101 (2017).
 - [14] A. Bohdan, J. Niemiec, O. Kobzar, and M. Pohl, *Astrophys. J.* **847**, 71 (2017).
 - [15] A. Spitkovsky, in *Astrophysical Sources of High Energy Particles and Radiation*, Vol. 801 (2005) pp. 345–350.
 - [16] A. Spitkovsky, *Astrophys. J.* **673**, L39 (2008).
 - [17] L. Sironi and A. Spitkovsky, *Astrophys. J.* **726**, 75 (2011).
 - [18] M. M. Leroy *et al.*, *Geophysical Research Letters* **8**, 1269 (1981).
 - [19] C. S. Wu, *Journal of Geophysical Research: Space Physics* **89**, 8857 (1984).
 - [20] L. Ball and D. B. Melrose, *Publications of the Astronomical Society of Australia* **18**, 361373 (2001).
 - [21] J. Park, C. Ren, J. C. Workman, and E. G. Blackman, *Astrophys. J.* **765**, 147 (2013), arXiv:1210.5654 [astro-ph.SR].
 - [22] M. A. Riquelme and A. Spitkovsky, *Astrophys. J.* **694**, 626 (2009), arXiv:0810.4565.
 - [23] D. Caprioli and A. Spitkovsky, *Astrophys. J.* **794**, 46 (2014), arXiv:1401.7679 [astro-ph.HE].
 - [24] A. R. Bell, *MNRAS* **353**, 550 (2004).
 - [25] B. Reville, J. G. Kirk, and P. Duffy, *Plasma Physics and Controlled Fusion* **48**, 1741 (2006), astro-ph/0608462.
 - [26] E. G. Zweibel and J. E. Everett, *Astrophys. J.* **709**, 1412 (2010), arXiv:0912.3511 [astro-ph.GA].
 - [27] E. M. Reynoso, J. P. Hughes, and D. A. Moffett, *AJ* **145**, 104 (2013), arXiv:1302.4678 [astro-ph.GA].
 - [28] P. Crumley, D. Caprioli, S. Markoff, and A. Spitkovsky, *MNRAS* **485**, 5105 (2019), arXiv:1809.10809 [astro-ph.HE].
 - [29] D. Caprioli, in *34th International Cosmic Ray Conference (ICRC2015)*, Vol. 34 (2015) p. 8, arXiv:1510.07042 [astro-ph.HE].
 - [30] M. Markevitch and A. Vikhlinin, *physrep* **443**, 1 (2007), astro-ph/0701821.
 - [31] R. J. van Weeren, H. J. A. Röttgering, M. Brüggen, and M. Hoeft, *Science* **330**, 347 (2010), arXiv:1010.4306 [astro-ph.CO].
 - [32] M. Ackermann, M. Ajello, A. Albert, *et al.*, *Astrophys. J.* **787**, 18 (2014), arXiv:1308.5654 [astro-ph.HE].
 - [33] G. Brunetti and T. W. Jones, *International Journal of Modern Physics D* **23**, 1430007-98 (2014), arXiv:1401.7519.
 - [34] T. N. Kato, arXiv e-prints, arXiv:1312.5507 (2013), arXiv:1312.5507 [physics.comp-ph].